Journal of Power Sources Advances 7 (2021) 100042

Contents lists available at ScienceDirect

Journal of Power Sources Advances

journal homepage: www.journals.elsevier.com/journal-of-power-sources-advances

Impact of catalyst layer morphology on the operation of high temperature PEM fuel cells

N. Bevilacqua [a], T. Asset [b], M.A. Schmid [a], H. Markötter [c,d], I. Manke [c], P. Atanassov [b], R. Zeis [a,*]

[a] Karlsruhe Institute of Technology (KIT) Helmholtz Institute Ulm (HIU), Helmholtzstraße 11, 89081, Ulm, Germany
[b] Department of Chemical and Biomolecular Engineering National Fuel Cell Research Center University of California, Irvine, CA, 92697, USA
[c] Helmholtz-Zentrum Berlin für Materialien und Energie (HZB), Hahn-Meitner-Platz 1, 14109, Berlin, Germany
[d] Bundesanstalt für Materialforschung und -prüfung (BAM), Unter den Eichen 87, 12205, Berlin, Germany

ARTICLE INFO

Keywords:
High-temperature polymer electrolyte membrane fuel cell
Platinum-free catalyst
Mass transport
Oxygen reduction reaction
Distribution of relaxation times analysis
Electrochemical impedance spectroscopy

ABSTRACT

Electrochemical impedance spectroscopy (EIS) is a well-established method to analyze a polymer electrolyte membrane fuel cell (PEMFC). However, without further data processing, the impedance spectrum yields only qualitative insight into the mechanism and individual contribution of transport, kinetics, and ohmic losses to the overall fuel cell limitations. The distribution of relaxation times (DRT) method allows quantifying each of these polarization losses and evaluates their contribution to a given electrocatalyst's depreciated performances. We coupled this method with a detailed morphology study to investigate the impact of the 3D-structure on the processes occurring inside a high-temperature polymer electrolyte membrane fuel cell (HT-PEMFC). We tested a platinum catalyst (Pt/C), a platinum-cobalt alloy catalyst (Pt_3Co/C), and a platinum group metal-free iron-nitrogen-carbon (Fe–N–C) catalyst. We found that the hampered mass transport in the latter is mainly responsible for its low performance in the MEA (along with its decreased intrinsic performances for the ORR reaction). The better performance of the alloy catalyst can be explained by both improved mass transport and a lower ORR resistance. Furthermore, single-cell tests show that the catalyst layer morphology influences the distribution of phosphoric acid during conditioning.

1. Introduction

PEMFCs have been extensively researched over the last years [1,2]. They hold promises to become a clean and compact electricity source for stationary to mobile applications. However, to achieve this goal, several challenges should be resolved. They range from managing the water at high current densities to the need for high purity gases, as impurities significantly affect the PEMFC performance, increasing their operating costs [3,4]. Operating PEMFCs above 120 °C overcomes many of these disadvantages as it eliminates liquid water from the system, therefore simplifying the water management, which reduces the complexity of the system.

Furthermore, the electrode kinetics are to be potentially faster. This effect is slightly compromised by the change in Gibbs free energy, which decreases linearly with increasing temperature. The elevated temperatures enable the system to run on steam reformates, as impurities (*e.g.* CO up to 3% in the anode gas stream) do not drastically impact the cell performance [5,6].

High-temperature PEMFCs (HT-PEMFCs) are usually operated at 160 °C. The proton conductivity of the conventional membrane, Nafion®, is reduced due to insufficient membrane hydration, induced by the absence of liquid water. Thus, HT-PEMFCs utilize a different proton-conducting membrane, namely phosphoric acid (H_3PO_4)-doped polybenzimidazole (PBI). In the catalyst layer, the liquid phosphoric acid conducts the protons to the reaction sites. Thus, the distribution of phosphoric acid inside the catalyst layer is vital for the triple-phase boundary and is key for the performance of the cell. Although various groups studied this issue in the past decade, it still requires a better understanding to achieve dynamic control of the triple-phase boundary [7–11]. The performance of the cell is further influenced by the catalytic activity of the cathode catalyst, where the oxygen reduction reaction (ORR) occurs. To improve its rate, platinum electrocatalysts (*e.g.* carbon-supported Pt nanoparticles, the state-of-the-art PEMFC cathode electrocatalyst) are often replaced by platinum-alloys, aiming to increase the ORR intrinsic activity through the strain-ligand and/or coarsening effects to reduce thereby the amount of the expensive platinum inside a

* Corresponding author. Institute of Technology (KIT), Helmholtz Institute Ulm (HIU), Helmholtzstraße 11, 89081, Ulm, Germany.
E-mail address: roswitha.zeis@kit.edu (R. Zeis).

https://doi.org/10.1016/j.powera.2020.100042
Received 31 July 2020; Received in revised form 18 November 2020; Accepted 24 November 2020

fuel cell [12–15]. Alloying platinum with 3d transition metal, such as nickel or cobalt, has proven to deliver the most significant improvement. For example, the Pt_3Co particles exhibit a Pt-rich surface layer with a reduced interatomic distance, which results in a modification of the Pt electronic structure and, thus, a decreased binding strength of the oxygen intermediate onto the catalytic surface. Furthermore, the non-noble part of the catalyst leaches out during operation, creating a rough catalyst surface. All these increase the reaction rate and the performance of the cell [15,16].

Further alternatives for conventional platinum catalysts are carbonaceous materials doped with atomically dispersed catalyst sites, often referred to as iron-nitrogen-carbon (Fe–N–C), which present the advantage being free of expensive and rare platinum group metals (PGMs). The electrode structure of the PGM-free catalyst has been thoroughly investigated by several groups [17–21]. They consist of a carbonaceous structure, composed of graphitic and amorphous domains with various types of moieties, either metal-free (*e.g.* pyridinic nitrogen, pyrrolic nitrogen, graphitic nitrogen, etc.) or M-N_x, the activity of which greatly depends on their coordination and their position in the carbon network. It is, however, often accepted that the M-N-C electrocatalysts should be designed while considering the $M-N_4$ moieties as the primary catalytic site for the ORR in PEMFCs, as they are usually found *in-plane*, in the mesopores and thus easily accessible, even in a solid electrolyte [22], by opposition to sites (*e.g.* Fe–N_{2+2}, N–Fe–N_{2+2}) which are present in the micropores and thus, exhibit low accessibility [21,23–26]. Notably, the oxygen diffusion in this type of catalyst is inhibited. Increased backpressure significantly boosts the performance of the cell, which indicates a mass transport issue [27]. During their operation in an HT-PEMFC, the reactants and reaction products need to be transported to and from the *in-plane* defects and, thus, navigate through the Fe–N–C complex network of meso (2–50 nm) and microporosities (<2 nm), hence requiring those defects to be in contact with the proton carrier, the viscous H_3PO_4. This process can be expected to inhibit the utilization of the catalyst sites, especially when considering that in conventional PEMFCs, Nafion® micelles with an average micelle size of 30 nm will also prevent proton transport in the smallest porosities [28]. This specific aspect is expected to be far less of a limitation when addressing PGM-group electrocatalysts, as the nanoparticles, ranging from 2 to 3 nm for pure-Pt and Pt-alloys to several dozens of nm for complex nanostructures, (*e.g.* Pt-based hollow nanoparticles [29], nanoframes [30], octahedra [31]) are far less likely to anchor/nucleate in the smallest porosities and are thus readily available for the reaction, exhibiting a lower transport resistance. However, the catalyst layer morphology plays a role in mass transport (MT) and Oxygen reduction reaction (ORR). Therefore it decisively influences the performance of the cell.

MT also includes the transport of protons to the reaction sites. Thus, the reaction sites need to be in contact with phosphoric acid to contribute to cell performance. An ideal wetting of the carbon support would include the smallest porosities, no flooding, and a thin film over the whole carbon support to optimize MT to the active sites. The proton conduction in the cathode is visible in the DRT spectrum of a HT-PEMFC [32]. Thus, different wetting behavior in catalysts with varying pore sizes can be observed using DRT.

X-ray tomographic methods were applied to investigate water transport in conventional PEMFCs to resolve MT phenomena in conventional PEMFCs [33]. These methods have been optimized over the years, and operando X-ray micro-computed tomography has been used to understand the water transport in Fe–N–C catalysts [34,35]. As the resolution of these techniques is insufficient to resolve the phosphoric acid distribution in nanometer-scaled pores of HT-PEMFC catalyst layers, operando X-ray micro-computed tomography is limited to a larger scale transport ways, such as cracks in the layered structure [36].

Several electrochemical impedance spectroscopy (EIS) studies on HT-PEMFCs were discussed in the literature [6,37–40]. They all found that hampered mass transport (MT) is responsible for severe polarization losses of the cell. To separate and quantify the different processes occurring inside the HT-PEMFC (*i.e.* reactant transport through the membrane or the porous network, charge transfer, *etc.*), we implemented the distribution of relaxation times (DRT) method, hence increasing our understanding of the cell's limitations. DRT has also been applied to analyze impedance spectra of other electrochemical systems such as solid oxide fuel cells by Schichlein et al. [41] and lithium-ion batteries [42]. Cuicci and Chen [43] developed a model to investigate the impedance spectra of PEMFCs, and Heinzmann et al. evaluated a conventional PEMFC [44]. A comprehensive overview of the development and application of the DRT method is presented by Dierickx et al. [45].

In our study, we allocated characteristic peaks of the spectrum to specific processes in a HT-PEMFC by varying the operating parameters of the cell. A typical fingerprint pattern is found for HT-PEMFCs equipped with various catalysts, which allows a direct comparison between cells [46]. Yezerska et al. [47] applied DRT analysis to artificially corroded catalysts to identify side-reactions. The spectrum of a low-temperature PEMFC shows unique characteristics different from those of a HT-PEMFC [44]. They mainly relate to the different morphology of the catalyst layer (*i.e.* higher thickness, PTFE as a binder instead of Nafion®) and the presence of phosphoric acid [32]. In this work, single-cell tests were performed with MEAs using various electrocatalysts. They belong to different groups: state-of-the-art Pt/C, Pt_3Co/C, and Fe–N–C. The cells exhibit a substantial performance gap, which could be explained by analyzing the impedance spectra coupled with DRT analysis. Furthermore, the results were linked to the morphology and the pore size distribution of the catalyst layers.

2. Experimental

2.1. Synthesis of the Fe–N–C catalyst

The Fe–N–C electrocatalysts were synthesized using the sacrificial support method (SSM). Namely, the precursors (i.e. $Fe(NO_3)_3{\cdot}9H_2O$ and Nicarbazin, from Sigma, LM-150, from Cabot, Ox-50, from Evonik and home-made Stöber Spheres) were mixed by wet impregnation overnight, before drying at 45 °C, a ball-milling (30 min, 45 Hz) and pyrolysis at 975 °C, for 45 min, under 7% H_2. The pyrolyzed material was ball-milled (30 min, 45 Hz) and etched in HF for four days to remove the silica (LM-150, Ox-50, and Stöber Spheres). Following the etching, the material was washed to neutral pH, dried, and pyrolyzed a second time, at 950 °C for 30 min, under 10% NH_3. The resulting electrocatalyst was ball-milled (1 h, 45 Hz) and used for the following characterizations.

2.2. Gas diffusion electrode fabrication

The fabrication process of the GDE influences catalyst distribution and needs to be optimized to obtain optimum performance [48,49]. Catalyst ink was prepared by mixing catalyst powder (Pt: 20 wt-% on Vulcan XC-72, Heraeus®; Pt_3Co: 30 wt-% on carbon black (undisclosed details), Tanaka; Fe–N–C: see above), IPA, and deionized water. The weight ratio of catalyst powder, IPA, and deionized water was 1:16:16. A 60 wt-% PTFE dispersion (TF 5060 GZ, 3 M™ Dyneon™) was added as a binder (7 wt-% of the dry electrode), and the dispersion was stirred for 2 h using a magnetic stirrer with a stir bar. The ink was subsequently spray-coated layer by layer onto a commercially available gas diffusion layer with a microporous coating (H2315–C2, Freudenberg®) at a temperature of 80 °C to dry the solvents during the coating process. The ink was sprayed using an airbrush system at an exuding pressure of 2 bar. The metal loading amounts to 1 $mg_{Pt}\,cm^{-2}$ in the Pt catalyst and 1 $mg_M\,cm^{-2}$ (M = metal) in the case of the Pt_3Co catalyst. The Fe–N–C catalyst loading was 3 $mg\,cm^{-2}$ (number represents the total weight of the catalyst). Catalyst loading was determined by weighing the dry gas diffusion electrode (GDE) after spray-coating. A more in-depth explanation of the GDE fabrication process was provided by Mack et al. [50,51]. The GDEs were cut into squares with a surface area of 4 cm^2 and laid on top of a stainless steel bipolar plate with serpentine gas flow channels with a

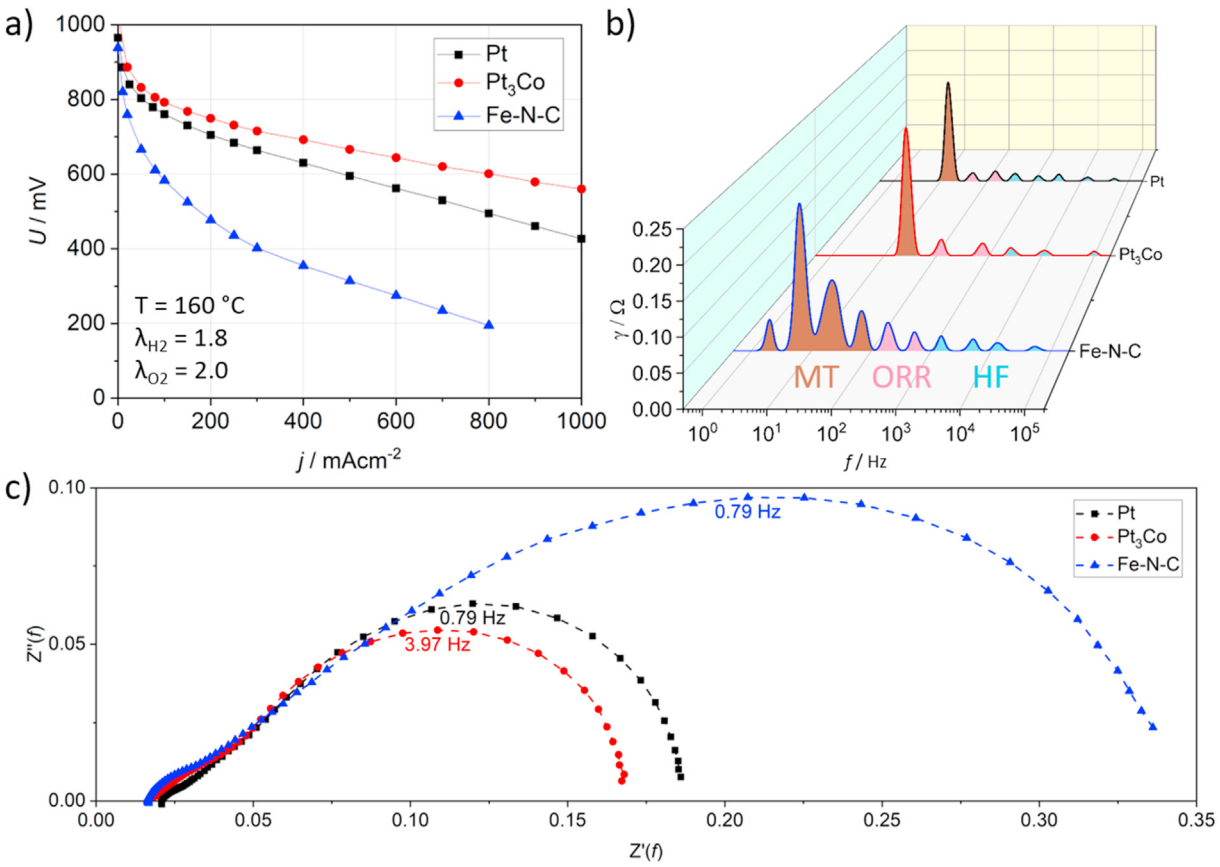

Fig. 1. Performance evaluation by all applied techniques of three investigated catalysts types. a) HFR-corrected polarization curves displaying the cell voltage *U* versus the applied current density *j*. b) distribution of relaxation times spectra. The frequency *f* is plotted versus the distribution function γ. c) Nyquist plots (real part Z′(*f*) vs. imaginary part Z''(*f*)) of electrochemical impedance at the same operating conditions ($\lambda_{H2} = 1.8$, $\lambda_{O2} = 2.0$, j = 100 mA cm^{-2}) for DRT and EIS. Apex frequency for the largest semi-circle is indicated with the label in the respective color. (For interpretation of the references to color in this figure legend, the reader is referred to the Web version of this article.)

width and depth of 1 mm each. The torque applied to eight screws was 2 Nm. They were fit into place by a PTFE gasket with a thickness of 220 μm to ensure that no gas is leaking and preventing cross-over. A PBI membrane (Dapozol® M40, Danish Power Systems) was doped for 14–28 days in concentrated phosphoric acid (85%, Normapur, VWR Chemicals) and sandwiched between the gas diffusion electrodes. In each cell, the anode was a standard Pt electrode with a loading of 1 mgPt cm^{-2}. This excess of anode loading was used to ensure that no operational limitations originate from the anode and ensure that the cathodic processes can be resolved without interference.

2.3. Cell operation

The conditioning of the assembled cells was achieved by heating them to 160 °C in a nitrogen atmosphere using heat pads and subsequently supplying them with hydrogen ($\lambda_{H2} = 1.8$) and air ($\lambda_{Air} = 2.0$) at ambient pressure (λ = stoichiometry). A current of 100 mA cm^{-2} was applied during the conditioning to ensure water production, which dilutes the phosphoric acid to facilitate proper acid distribution and to keep the cell voltage at a non-corrosive potential. During activation, polarization curves and impedance spectra were recorded after 2 h and every 24 h. After 120 h, each cell reached (or has already reached) a steady cell voltage, and the activation was finished. After conditioning, operation parameters were changed to monitor the response of the fuel cell. The parameters were in all cases varied at least 30 min before recording an impedance spectrum and a polarization curve to give the system enough time to equilibrate and to ensure that the EIS captures only steady-state phenomena. Where specified, oxygen was chosen as the cathode reactant gas. The stoichiometry on the cathode side was varied between λ = 2.0, 5.0, and 10.0 for both air and oxygen. The hydrogen stoichiometry was always kept constant at $\lambda_{H2} = 1.8$.

2.4. Electrochemical impedance spectroscopy

Impedance spectra were recorded after an equilibration period of 30 min using a Zahner Zennium (Zahner Elektrik) workstation connected to a Zahner Power Pack 211, which supplied the current. The frequency range over which the data was collected was 100 kHz to 50 mHz, at a rate of 10 points per decade and 6 repetitions for each point. This range successfully captures all frequencies at which fast processes such as the hydrogen oxidation reaction and proton transport, and slow processes such as oxygen diffusion and the oxygen reduction reaction occur.

2.5. Distribution of relaxation times analysis

The resulting impedance spectra were further analyzed using the distribution of relaxation times analysis with the open-source toolbox DRTtools [52]. Quantification of each process's contribution to the overall impedance of the cell was achieved by calculating the area under each peak. The attribution of each peak to a process inside the fuel cell has been accomplished by Weiβ et al. [37]. The slowest processes (within the frequency range until 50 mHz as mentioned earlier) is attributed to oxygen mass transport (MT) and typically range from 1 Hz to 15 Hz. For Pt and Pt_3Co catalysts, MT is characterized by one peak that is usually higher than the other peaks. The oxygen reduction reaction (ORR) results in two peaks between 15 Hz and 150 Hz, and typically above 150 Hz, the

high frequency (HF) area is found, which includes the hydrogen oxidation reaction and proton transport in the catalyst layer. The frequency range of a DRT spectrum might shift due to pressure fluctuations or if the time constants of the internal processes vary. The frequency ranges mentioned above are not rigid borders, the latter being described by the peaks in the spectrum more than the values mentioned hereinto. Thus, each cell is rather classified by a fingerprint pattern. DRT spectra of HT-PEMFC are described in more detail in the literature [32,37,46].

2.6. Morphology characterization

To investigate the three-dimensional structure of the catalysts, high-resolution sorption measurements (3Flex, Micromeritics®) and high-resolution focussed ion beam scanning electron microscopy (FIB-SEM) tomography were conducted [53]. The nitrogen sorption was used to characterize the pores with a diameter below 100 nm. The device was equipped with a special micropore port and a 0.1 Torr pressure transducer. The samples were outgassed at 160 °C for 4 h. Classical macroscopic theories typically lead to an underestimation of pore sizes in micropores and mesopores [54]. To account for the inaccuracy of BET at low pore diameters, the differential pore surface area was calculated using the Non-Local Density Functional Theory (NLDFT) method with the assumption of cylindrical pore shape. The NLDFT describes the sorption behavior of fluids in the vicinity of curved walls, such as in micropores, on a molecular level and is hence more accurate than macroscopic approaches [55,56]. The NLDFT method used in this work is built into the analysis software 3Flex® of the Micromeritics® device.

FIB-SEM images of the Pt catalyst and the Pt_3Co catalyst were recorded at Helmholtz-Zentrum Berlin (Zeiss Crossbeam 340 gallium FIB with a Gemini column). The edge length of each voxel amounts to 5 nm in all dimensions, the electrons were accelerated with a voltage of 3 kV, and the secondary electrons were detected. The ablation was achieved with a FIB current of 700 pA. The images were translated into a pore network representing the void phase of the porous carbon flakes, and the pore size distribution was analyzed with a watershed-based algorithm using a code written by Gostick [57]. The pore size distribution was created using the open-source pore network modeling software OpenPNM [58]. A more detailed explanation of this process can be found in the literature [7,8].

3. Results and discussion

3.1. Normal operation

To understand the connection between all three applied techniques, Fig. 1 presents a comparison of the polarization curves (a), the DRT spectra (b), and the Nyquist plots of all three investigated catalysts (c). Fig. 1a shows the polarization curves of the cells operated with hydrogen ($\lambda_{H2} = 1.8$) and oxygen ($\lambda_{O2} = 2.0$) as fuel gases. The Pt_3Co alloy catalyst (red) performs better than the standard Pt catalyst, in agreement with the literature [12–15]. The Fe–N–C performs worse than the PGM-containing catalysts. Without further characterization, it is impossible to determine the cause of the performance differences between the three catalysts. However, the first assumption would be to assess them to the lower intrinsic activity of the Fe–N–C electrocatalysts. The ohmic regions of the HT-PEMFC typically occur at current densities (j) higher than 400 mA cm^{-2}, at which the mass transport already affects the performance of the cell. Hence, the ohmic region is expected to be influenced by membrane resistance and oxygen mass transport inside the cell. In our setup for HT-PEMFCs, no typical logarithmic decline of the polarization curve can be observed, even at 2000 mA cm^{-2}. Thus, substantial mass transport limitation cannot be excluded solely by the polarization curve.

To determine the exact cause of the performance differences, EIS and subsequent DRT analysis of the impedance spectra was performed. The impedance shown in Fig. 1c displays an increased mid to low frequency resistance for the Fe–N–C catalyst (blue). The cell employing the Pt_3Co catalyst (red) shows a decreased mid to low frequency resistance compared to the standard Pt cell (black). Minor differences of the high-frequency onset (Z" (f) = 0) originate from variations in the membrane resistance. The high-frequency region of the EIS shows similarities between all three catalysts, as it originates from proton conduction in the catalyst layer and the anode, which is the same electrode (1 mgPt cm^{-2}) in all cases.

The DRT spectrum (Fig. 1b) exhibits the fingerprint pattern mentioned above for the commercial PGM catalysts with porous carbon powder-based substrates. The pattern for the Pt catalyst (black) shows one dominant mass transport peak at low frequencies (1–15 Hz), followed by two oxygen reduction reaction peaks at medium frequencies (15–150 Hz) and several peaks at higher frequencies (>150 Hz). The shape and allocation of this pattern to the various fuel cell processes are found in greater detail in the literature [32,37]. The same fingerprint is observed in the Pt_3Co catalyst (red). However, the mass transport peak is narrower, and the second ORR peak is shifted toward higher frequencies (up to 500 Hz). This shift is caused by faster reaction kinetics and is consistent with the observed ORR performance of this catalyst [12–15]. As mentioned earlier, a change of frequencies in the DRT can occur by varying time constants of the respective process. The DRT spectrum of the Fe–N–C shows similar features as the standard cell. We, therefore, assume that the processes occurring in both cells do not differ significantly. The Pt_3Co system outperforms the standard Pt catalyst, which translates into a smaller Nyquist plot with a higher apex frequency. The apex frequency indicates that the process which is limiting the performance the most (oxygen mass transport) is faster. This fact is confirmed by the more accurate DRT method, in which the MT peak of Pt_3Co/C occurs at a higher frequency. DRT analysis further shows that the higher performance originates from both the facilitated mass transport (*ca.* 30% decrease *vs.* Pt/C) and the improved ORR kinetics (*ca.* 50% *vs.* Pt/C) of the alloyed system. The improved MT is surprising at first glance since both platinum-based nanoparticles are supported on carbon black. The improvement might arise from a different morphology of the supports (*i.e.* Vulcan XC72 for Pt/C *vs.* undisclosed carbon black support for Pt_3Co/C). This discrepancy is to be further elaborated in Section 3.2.

The DRT spectrum of the Fe–N–C (blue) catalyst clearly shows a similar fingerprint as the PGM-containing catalysts. Thus, the processes occurring inside this type of catalyst can be assumed to be identical, and the time scales do overlap. Further, the change of the peaks in the DRT spectrum during conditioning (see Fig. S1) indicates that the mass transport regime for this type of catalyst occurs at 1–100 Hz. The peaks describing the oxygen reduction reaction occur at 100–600 Hz. A distinction of the DRT spectrum of the Fe–N–C catalyst is that the low-frequency region of the DRT Fe–N–C catalyst spectrum exhibits multiple peaks, indicating a change of the mass transport process inside the cell. The EIS also does not show a semi-circle at low frequencies, which is why the DRT method fits more than one peak to describe the MT. The low-frequency resistance is dominating for all three catalysts, but this effect is exacerbated for the Fe–N–C catalyst. That indicates that for many catalyst sites, the H_3PO_4 and oxygen have difficulties accessing them (*e.g.*, in micropores or other small porosities), such as the Fe–N_{2+2} or Fe–N_2 sites. This explanation confirms the statement in the introduction that catalyst sites in the micropores are detrimental due to their poor accessibility. Compared to Pt/C and Pt_3Co/C, the distribution of catalyst

Table 1
Resistances obtained from DRT analysis of the three investigated catalysts operating with oxygen at 100 mA cm^{-2} and power density at 200 mA cm^{-2} after conditioning. The maximum power density has not been reached for these cells at 1000 mA cm^{-2}.

	Pt/C	Pt_3Co/C	Fe–N–C
Mass transport resistance/mΩ	88.7	26.5	243.7
Oxygen reduction reaction resistance/mΩ	24.2	11.8	61.9
High frequency resistance/mΩ	13.4	13.3	18.4
Power density @ 200 mA cm^{-2}/mW cm^{-2}	35.3	37.5	23.9

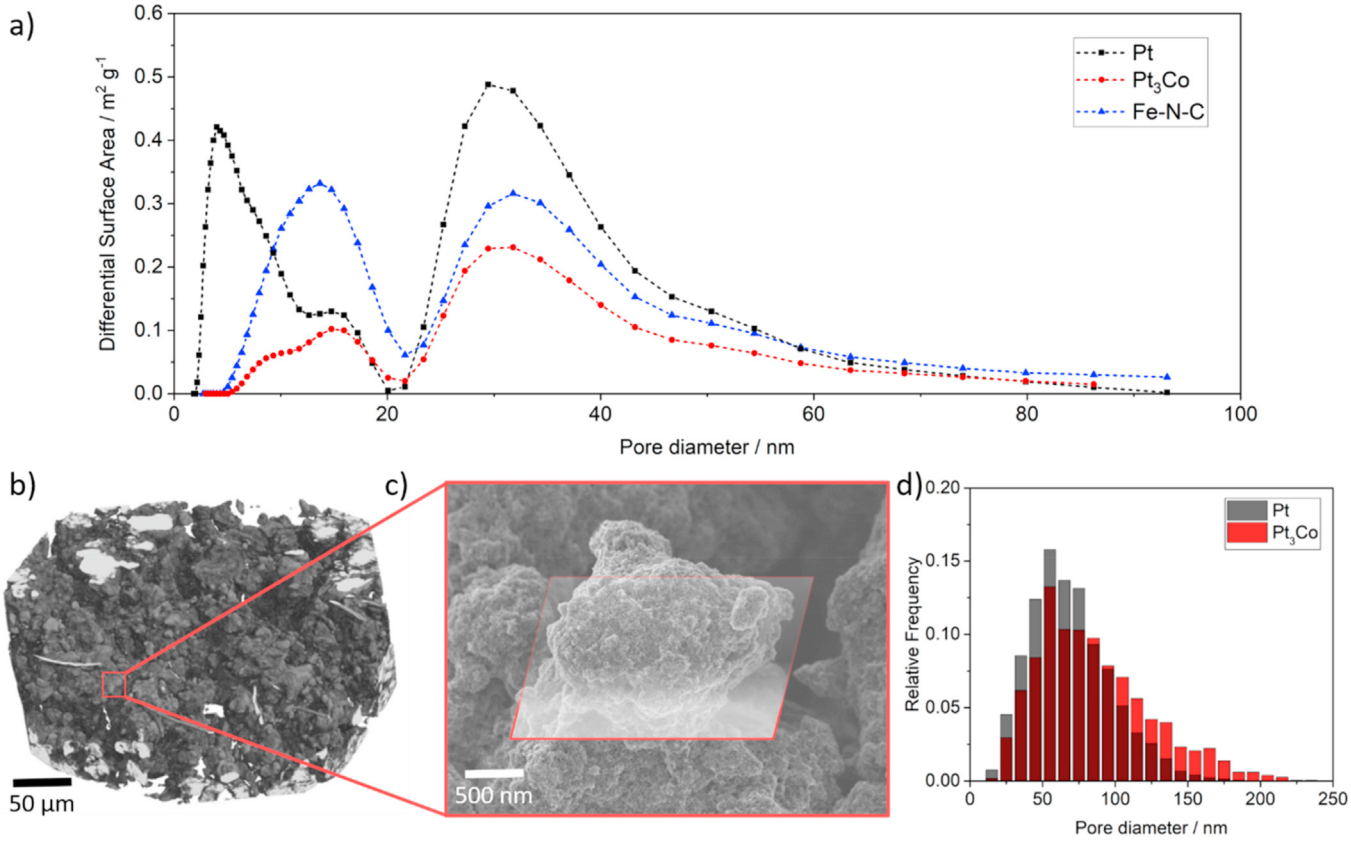

Fig. 2. (a) Differential pore surface area from all three catalyst powders obtained from the sorption measurements. (b) Sample 3D X-ray micro-computed tomogram of the catalyst showing the micrometer scale of the catalyst layer. (c) SEM image of the highlighted portion, showing one carbon flake (nanometer scale). The region of interest for FIB-SEM imaging is shown in red. (c) The pore size distribution of nanoscale pores diameters obtained by extracting a pore network from FIB-SEM data [57]. The Pt catalyst is shown in black, the Pt_3Co catalyst is colored in red. (For interpretation of the references to color in this figure legend, the reader is referred to the Web version of this article.)

sites in Fe–N–C [21,23] aggravates the negative influence of a suboptimal impregnation of the electrode by phosphoric acid. As mentioned in the introduction, the Pt and Pt_3Co nanoparticles (2–3 nm) are less likely to anchor or nucleate inside micropores and exhibit much higher accessibility than the micropores sites in Fe–N–C electrocatalysts. The high-frequency resistance of the Fe–N–C catalyst is increased as well, according to both the cell voltage decreases at 100 mA cm^{-2} and the EIS/DRT signals, further indicating depreciated kinetics *vs.* Pt and Pt_3Co/C. Overall, the hampered mass transport and kinetics for Fe–N–C translates into additional peaks in the DRT spectrum. The quantitative results of the DRT spectrum recorded during regular operation are shown in Table 1. The mentioned limitations, the mass transport and ORR charge transfer resistances, are, for Fe–N–C, increased by a factor of *ca.* 2.5 *vs.* Pt/C.

3.2. Catalyst layer morphology

Fig. 2a shows the differential pore surface area in the catalyst powders obtained with sorption experiments from 2 nm–93 nm pore diameter. All three catalysts exhibit a hierarchical pore structure with pores below and above 20 nm in diameter and a minimum at 20 nm. The Pt catalyst has the highest fraction of pore surface area below 20 nm (67% of the total surface area) compared to Pt_3Co (44%) and Fe–N–C (61%). We expect slower oxygen diffusion in smaller pores. The DRT analysis confirms that substantially fewer small pores (below 20 nm) of the Pt_3Co catalyst benefit the fuel cell performance by reducing the mass transport resistance, as discussed in Section 3.1. This result further indicates that the catalytic particles located in the smallest pores participate in the reaction, as they contribute to the EIS. Consequently, H_3PO_4 invades these small pores and establishes the triple-phase boundary also in these regions.

To further elucidate the difference between the Pt/C and Pt_3Co/C, which are of similar types (Pt deposited on a carbon powder support), and obtain more information about pores between 100 nm and 250 nm, a 3D FIB-SEM image has been recorded. FIB-SEM images of Pt/C and Pt_3Co/C are shown in the supplementary information in Fig. S5. FIB-SEM images of the Fe–N–C catalyst were previously published by Stariha et al. [19]. The region of interest is shown in Fig. 2b and c. A sample 3D X-ray micro-computed tomogram is shown in Fig. 2b to indicate the hierarchical pore structure. The porous support material exhibits pores in the micrometer range, but the individual carbon flakes shown in Fig. 2c are porous themselves and exhibit pores on the nanometer scale. One such flake was ablated using FIB-SEM to create a 3D image of the nanometer pore space. The resulting pore size distribution is shown in Fig. 2c. The relative frequency analysis confirms the lower amount of small pores in the Pt_3Co catalyst layer. It exhibits more pores with a diameter greater than 100 nm, in which we expect the oxygen diffusion to be faster. The substrate of the Pt_3Co catalyst contains 7% of pores larger than 150 nm in diameter, compared to 1% for the support of the Pt catalyst.

Further, the mean pore size is *ca.* 83 nm for Pt_3Co/C and *ca.* 61 nm for Pt/C. The larger pores facilitate the transport of both the reactant gas and the phosphoric acid. This improves oxygen diffusion by supplying the reactive sites more effectively with oxygen and explains the decrease of the MT in the DRT spectrum. The ORR resistance decrease is defined by the higher intrinsic catalytic activity of Pt_3Co *vs.* Pt (confirmed by RDE measurements shown in Fig. S2 in the supplementary information) and the improved mass transport, which increases the oxygen concentration at the catalyst sites. Hence, the MT and the ORR correlate.

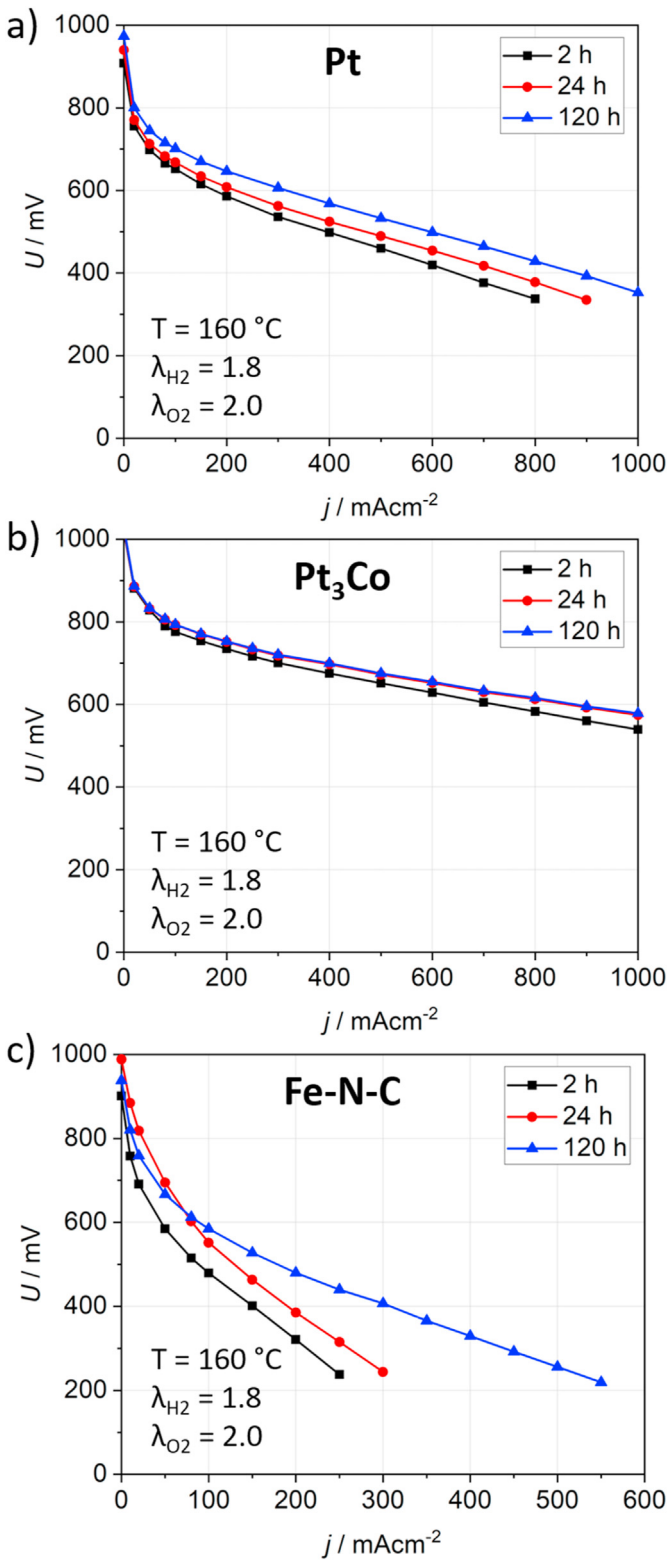

Fig. 3. HFR-corrected polarization curves (a–c) of all three catalysts taken during the conditioning period of the cell, after 2 h (black), after 24 h (red), after 120 h (blue). All cells are conditioned at 100 mA cm^{-2}. *U* represents the cell voltage, and *j* represents the applied current density. (For interpretation of the references to color in this figure legend, the reader is referred to the Web version of this article.)

3.3. Conditioning of the fuel cells

The cells were conditioned over a period of 120 h. After 2 h and subsequently every 24 h of operation, polarization curves and impedance spectra were recorded. Fig. 3a–c shows the cell performance during conditioning of the fuel cells at 100 mA cm^{-2}. For the sake of clarity, only three data sets are presented: 2 h, 24 h, 120 h (a complete version of the resistance evolutions is illustrated in Fig. 4). The standard Pt/C cell reached its peak performance (peak performance = within 3 mV of the cell performance after 120 h) after 72 h of operation, whereas the Pt_3Co/C cell conditioned faster. After 24 h, it already reached its peak performance. The total cell voltage increase during conditioning is higher for Pt/C compared to Pt_3Co/C. Both cells show similar behavior, as the increase at higher current densities is more pronounced while the phosphoric acid is still distributed within the pores. Initially, the amount of catalyst particles is insufficient to maintain a high current density. This issue results in an additional overpotential at high current density, which is overcome once the acid is distributed more evenly. The Fe–N–C catalyst shows the highest increase in performance. The increase at high current density is especially noticeable, implying that the contribution of the catalyst inside the smallest porosities gradually increases during activation, as a result of their better impregnation by H_3PO_4. This explanation is confirmed by Fig. 4, in which the MT resistance and the ORR resistance of the fuel cells during conditioning are shown. The Fe–N–C conditioning is not finished after 120 h of operation, which further highlights the difficulty of phosphoric acid to perchlorate into the catalyst layer. The graphs in Fig. 4 still decrease for both MT and ORR. In the case of Pt/C, the conditioning is finished after 120 h. At this point, the MT resistance and the ORR resistance reach a minimum, and the activation process is completed as the cell reached its maximum performance. Similar values for conditioning time were reported in the literature [59]. For Pt_3Co/C, the conditioning was already finished after 24 h.

MT and ORR resistances remain at a constant low after this time, and we assume that the distribution of phosphoric acid in the catalyst layer is homogeneous. The variation, as mentioned earlier in pore sizes, can explain this time discrepancy. The large pores facilitate a thorough impregnation. The shape of the DRT spectrum (Fig. S1) confirms that the nature of the internal processes does not change during conditioning of the cells, with the sole exception of Pt_3Co/C. The ORR peaks of the Pt_3Co catalyst show a peak growing at 100 Hz–300 Hz. We hypothesize that this peak (allocated to the ORR) might arise due to a change in the surface composition of the alloyed nanoparticles (*i.e.* switch from Pt_3Co to Pt_3Co@Pt core@shell [60], Pt-skeleton [61] or Pt-hollow [29]), which alters the nature of the ORR, especially concerning the time constant at which the reaction is taking place. This process is described frequently in the literature [62–65].

The impact of the morphology of the catalyst layer is still palpable after the conditioning of the fuel cells. In the case of the Pt/C catalyst, the MT resistance and the ORR resistance are both higher compared to the Pt_3Co/C catalyst. This observation indicates that the activity of platinum particles in the nanometer-scaled pores is hampered by the poor H_3PO_4 distribution and the oxygen diffusion inside these pores. Additionally, the shorter activation phase in the Pt_3Co/C catalyst case also confirms this. We hypothesize that the non-ideal acid distribution leads to dead zones in the smallest nanometer-scale pores of the catalyst. The nanoparticles are there not in contact with phosphoric acid. Thus, they do not participate in the performance of the fuel cell, even after conditioning. Fig. 5 shows a schematic representation of the phosphoric acid distribution before and after activation. The white background in Fig. 5 indicates the smallest nanometer-scaled areas. For the Fe–N–C catalyst, the $Fe–N_{2+2}$ catalyst sites are located dominantly in the nanometer-scaled pores. The activity of these catalytic sites is crucial for high performance, and thus, the impact of the morphology is even more substantial in this type of catalyst. The light blue background indicates smaller nanometer-scale pores (below 20 nm) in contact only after conditioning

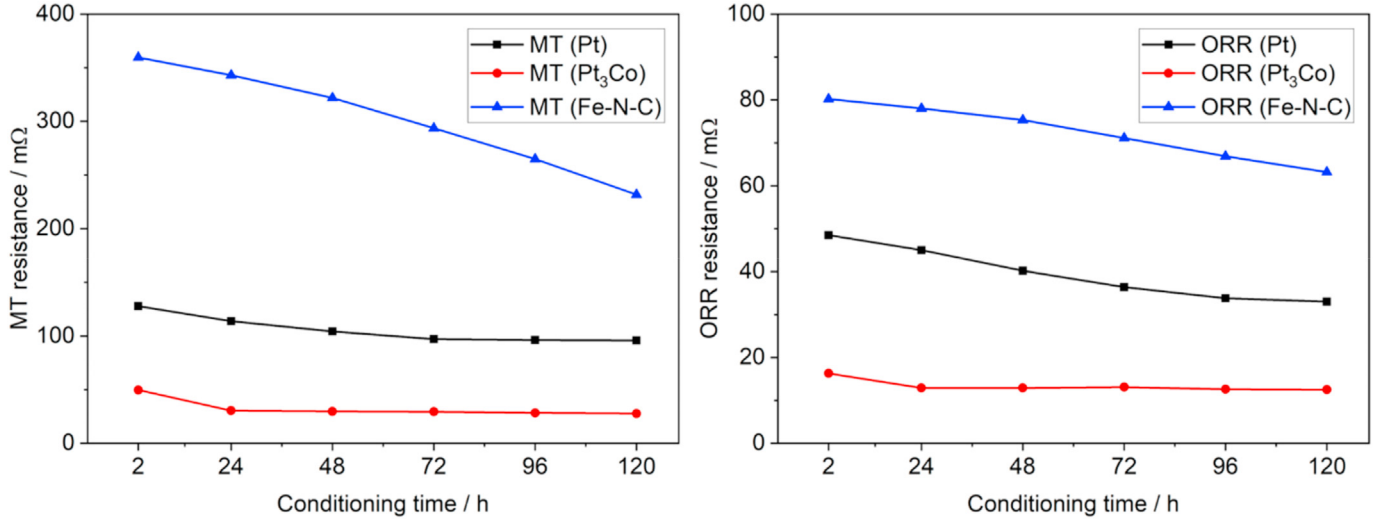

Fig. 4. MT resistance (solid lines) and ORR resistance (dashed lines) for the catalysts during conditioning of the cells. The numbers are obtained from DRT analysis.

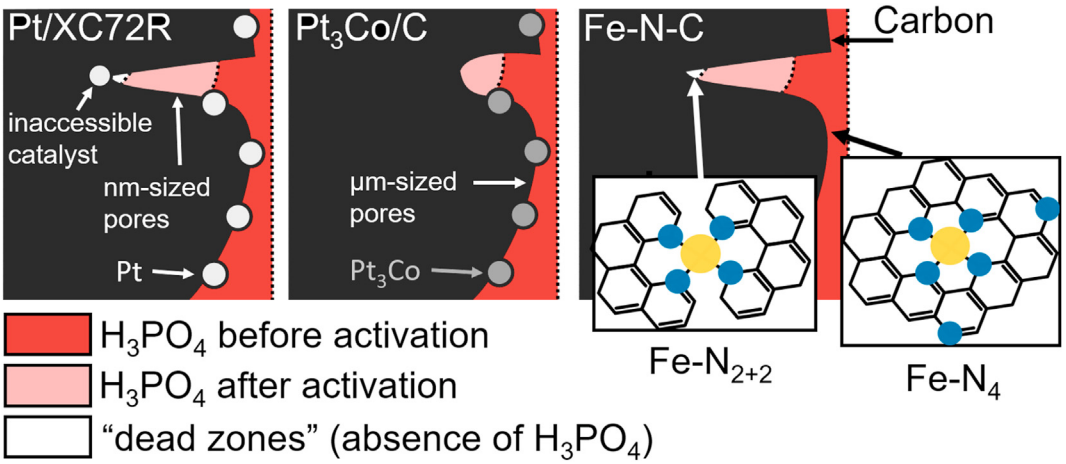

Fig. 5. Schematic representation of the pore space of all three investigated catalyst types during activation. The blue background indicates the phosphoric acid distribution before the activation phase (dark blue) and after activation (light blue). The white background depicts areas in which no phosphoric acid transport is expected. (For interpretation of the references to color in this figure legend, the reader is referred to the Web version of this article.)

and in which catalytic sites are located in all three investigated catalysts. These sites contribute to the cell's performance after conditioning, and they exhibit a substantial MT resistance. The Pt/C catalyst structure includes more of these pores compared to the Pt_3Co/C system. Thus, the observed MT is higher in the Pt/C system. However, the performance gap is not as significant as the gap of the Fe–N–C catalyst. As the Pt3Co/C system exhibits few small nanometer-scale pores, the MT is the lowest. The accelerated conditioning indicates that the wetting of these larger pores with phosphoric acid is facilitated. We assume that more catalytic particles can contribute to cell performance in addition to improved mass transport. The extent to which each effect impacts the performance can not be singled out. Whether an improved wetting in the small nanometer-scale pores or the absence of nanometer-scale pores is more effective in increasing the overall catalyst performance needs to be determined further.

4. Conclusions

This study investigated three different types of HT-PEMFC cathode catalyst: Pt/C, Pt_3Co/C, Fe–N–C. Each catalyst was implemented into MEA and characterized by polarization curves, EIS, and DRT analysis. A typical DRT fingerprint pattern is observed for each catalyst type. We found that there is a significant performance gap between these types of catalysts, which can be explained by (i) the intrinsic activity of each electrocatalyst for the oxygen reduction reaction (i.e. $Pt_3Co > Pt >$ Fe–N–C) and (ii) the morphology of the catalyst layer. The latter was determined by sorption experiments and extracting a 3D pore network from FIB-SEM nano-tomography measurements. The conditioning of the fuel cells highlights the impact of the morphology, as the time needed to reach close-to-optimal performances strongly correlates with the phosphoric acid distribution inside the porous catalyst layer. An electrocatalyst with a large average pore size (*e.g.* the Pt_3Co catalyst with *ca.* 83 nm average pore size *vs. ca.* 68 nm for Pt) facilitates the acid distribution. It shortens the activation period of the fuel cell. The Fe–N–C catalyst experiences the slowest conditioning phase (>120 h), as it requires the H_3PO_4 to access not only its small mesopores but also its micropores where part of its catalyst sites is found. Through the use of DRT, we were able to deconvolve the contribution of mass transport and ORR kinetics on a given electrocatalyst activity in HT-PEMFC. Therefore, it is emphasizing the fact that mass-transport plays a critical role in the design of such systems.

Declaration of competing interest

The authors declare that they have no known competing financial interests or personal relationships that could have appeared to influence the work reported in this paper.

Acknowledgments

Special thanks go to Angela Straβ-Eifert for the sorption measurements. We acknowledge the "Impuls-und Vernetzungsfonds der Helmholtz Gesellschaft" for the financial support (Young Investigator Group project VH-NG-616) and the "Zentrum für Sonnenenergie-und Wasserstoff-Forschung Baden-Württemberg" (ZSW) for providing the infrastructure. This work contributes to the research performed at CELEST (Center for Electrochemical Energy Storage Ulm-Karlsruhe).

Appendix A. Supplementary data

Supplementary data to this article can be found online at https://doi.org/10.1016/j.powera.2020.100042.

References

[1] R. Zeis, Materials and characterization techniques for high-temperature polymer electrolyte membrane fuel cells, Beilstein J. Nanotechnol. 6 (2015) 68–83.
[2] A. Chandan, M. Hattenberger, A. El-kharouf, D. Shangfeng, A. Dhir, V. Self, et al., High temperature (HT) polymer electrolyte membrane fuel cells (PEMFC) - a review, J. Power Sources 231 (2013) 264–278.
[3] Y. Chang, Y. Qin, Y. Yin, J. Zhang, X. Li, Humidification strategy for polymer electrolyte membrane fuel cells - a review, Appl. Energy 230 (2018) 643–662.
[4] G. Wang, Y. Yu, H. Liu, C. Gon, S. Wen, X. Wang, et al., Progress on design and development of polymer electrolyte membrane fuel cell systems for vehicle applications: a review, Fuel Process. Technol. 179 (2018) 203–228.
[5] J.S. Wainright, J.-T. Wang, D. Weng, R.F. Savinell, M. Litt, Acid-doped polybenzimidazoles: a new polymer electrolyte, J. Electrochem. Soc. 142 (7) (1995) L121–L123.
[6] J. Zhang, Z. Xie, J. Zhang, Y. Tang, C. Song, T. Navessin, et al., High temperature PEM fuel cells, J. Power Sources 160 (2006) 872–891.
[7] N. Bevilacqua, M.G. George, S. Galbiati, A. Bazylak, R. Zeis, Phosphoric acid invasion in high temperature PEM fuel cell gas diffsuion layers, Electrochim. Acta 257 (2017) 89–98.
[8] S. Chevalier, M. Fazeli, F. Mack, S. Galbiati, I. Manke, A. Bazylak, et al., Role of the microporous layer in the redistribution of phosphoric acid in high temperature PEM fuel cell gas diffusion electrodes, Electrochim. Acta 212 (2016) 187–194.
[9] Y. Oono, A. Sounai, M. Hori, Influence of the phosphoric acid-doping level in a polybenzimidazole membrane on the cell performance of high-temperature proton exchange membrane fuel cells, J. Power Sources 189 (2009) 943–949.
[10] C. Wannek, I. Konradi, J. Mergel, W. Lehnert, Redistribution of phosphoric acid in membrane electrode assemblies for high-temperature polymer electrolyte fuel cells, Int. J. Hydrogen Energy 34 (2009) 9479–9485.
[11] S. Yu, L. Xiao, B.C. Benicewicz, Durability studies of PBI-based high temperature PEMFCs, Fuel Cell. 3–4 (2008) 165–174.
[12] E. Antolini, J.R.C. Salgado, E.R. Gonzalez, The stability of Pt-M (M = first row transition metal) alloy catalysts and its effect on the activity in low temperature fuel cells A literature review and tests on a Pt-Co catalyst, J. Power Sources 160 (2006) 957–968.
[13] H.R. Colón-Mercado, B.N. Popov, Stability of platinum based alloy cathode catalysts in PEM fuel cells, J. Power Sources 155 (2006) 253–263.
[14] Y. Qian, W. Wen, P.A. Adcock, Z. Jiang, N. Hakim, M.S. Saha, et al., PtM/C catalyst prepared using reverse micelle method for oxygen reduction reaction in PEM fuel cells, J. Phys. Chem. C 112 (2008) 1146–1157.
[15] C.V. Rao, J. Parrondo, S.L. Ghatty, B. Rambabu, High temperature polymer electrolyte membrane fuel cell performance of Pt_xCo_y/C cathodes, J. Power Sources 195 (2010) 3425–3430.
[16] H.A. Gasteiger, S.S. Kocha, B. Sompalli, F.T. Wagner, Activity benchmarks and requirements for Pt, Pt-alloy, and non-Pt oxygen reduction catalysts for PEMFCs, Appl. Catal. B Environ. 56 (2005) 9–35.
[17] H.T. Chung, D.A. Cullen, D. Higgins, B.T. Sneed, E.F. Holby, K.L. More, et al., Direct atomic-level insight into the active sites of a high-performance PGM-free ORR catalyst, Science 357 (2017) 479–484.
[18] A. Serov, M.J. Workman, K. Artyushkova, P. Atanassov, G. McCool, S. McKinney, et al., Highly stable precious metal-free cathode catalyst for fuel cell application, J. Power Sources 327 (2016) 557–564.
[19] S. Stariha, K. Artyushkova, M.J. Workman, A. Serov, S. McKinney, B. Halevi, et al., PGM-free Fe-N-C catalysts for oxygen reduction reaction: catalyst layer design, J. Power Sources 326 (2016) 43–49.
[20] J.O. Jensen, D. Aili, Y. Hu, L.N. Cleemann, Q. Li, High-temperature polymer electrolyte membrane fuel cells, in: N. Nakashima (Ed.), Nanocarbons for Energy Conversion: Supramolecular Approaches, Springer, Cham, 2019, pp. 45–79.
[21] M.J. Workman, A. Serov, L-k Tsui, P. Atanassov, K. Artyushkova, Fe-N-C catalyst graphitic layer structure and fuel cell performance, ACS Energy Letters 2 (2017) 1489–1493.
[22] L. Zhong, J.O. Jensen, L.N. Cleemann, C. Pan, Q. Li, Electrochemical probing into the active sites of grpahitic-layer encapsulated iron oxygen reduction reaction electrocatalysts, Sci. Bull. 63 (1) (2017) 24–30.
[23] A. Serov, K. Artyushkova, P. Atanassov, Fe-N-C oxygen reduction fuel cell catalyst derived from carbendazim: synthesis, structure, and reactivity, Advanced Energy Materials 4 (2014) 7.
[24] T. Asset, P. Atanassov, Iron-nitrogen-carbon catalysts for proton exchange membrane fuel cells, Joule 4 (1) (2020) 33–44.
[25] Y. Qian, Z. Liu, H. Zhang, P. Wu, C. Cai, Active site structures in nitrogen-doped carbon-supported cobalt catalysts for the oxygen reduction reaction, ACS Appl. Mater. Interfaces 8 (48) (2016) 32875–32886.
[26] F. Jaouen, M. Lefèvre, J.-P. Dodelet, M. Cai, Heat-treated Fe/N/C catalysts for O2 electroreduction: are active sites hosted in micropores? J. Phys. Chem. B 110 (2006) 5553–5558.
[27] R. Gokhale, T. Asset, G. Qian, A. Serov, K. Artyushkova, B.C. Benicewicz, et al., Implementing PGM-free electrocatalysts in high-temperature polymer electrolyte membrane fuel cells, Electrochem. Commun. 93 (2018) 91–94.
[28] A. Serov, A.D. Shum, X. Xiao, V. De Andrade, K. Artyushkova, I.V. Zenyuk, et al., Nano-structured platinum group metal-free catalysts and their integration in fuel cell electrode architectures, Appl. Catal. B Environ. 237 (2018) 1139–1147.
[29] L. Dubau, T. Asset, R. Chattot, C. Bonnaud, V. Vanpeene, J. Nelayah, et al., Tuning the performance and the stability of porous hollow PtNi/C nanostructures for the oxygen reduction reaction, ACS Catal. 5 (2015) 5333–5341.
[30] C. Chen, Y. Kang, Z. Huo, Z. Zhu, W. Huang, H.L. Xin, et al., Highly crystalline multimetallic nanoframes with three-dimensional electrocatalytic surfaces, Science 343 (6177) (2014) 1339–1343.
[31] C. Cui, L. Gan, H.-H. Li, S.-H. Yu, M. Heggen, P. Strasser, Octahedral PtNi nanoparticle catalysts: exceptional oxygen reduction activity by tuning the alloy particle surface composition, Nano Lett. 12 (2012) 5885–5889.
[32] N. Bevilacqua, M.A. Schmid, R. Zeis, Understanding the role of the anode on the polarization losses in high-temperature polymer electrolyte membrane fuel cells using the distribution of relaxation times analysis, J. Power Sources 471 (2020) 228469.
[33] A. Bazylak, Liquid water visualization in PEM fuel cells: a review, Int. J. Hydrogen Energy 34 (2009) 3845–3857.
[34] J. Liu, M.R. Talarposhti, T. Asset, D.C. Sabarirajan, D.Y. Parkinson, P. Atanassov, et al., Understanding the role of interfaces for water management in platinum group metal-free electrodes in polymer electrolyte fuel cells, ACS Appl. Energy Mater. 2 (2019) 3542–3553.
[35] S.J. Normile, D.C. Sabarirajan, O. Calzada, V. De Andrade, X. Xiao, P. Mandal, et al., Direct observations of liquid water formation at nano- and micro-scale in platinum group metal-free electrodes by operando X-ray computed tomography, Materials Today Energy 9 (2018) 187–197.
[36] J. Halter, N. Bevilacqua, R. Zeis, T.J. Schmidt, F.N. Büchi, The impact of the catalyst layer structure on phosphoric acid migration in HT-PEFC - an operando X-ray tomographic microscopy study, J. Electroanal. Chem. 859 (2020) 113832.
[37] A. Weiß, S. Schindler, S. Galbiati, M.A. Danzer, R. Zeis, Distribution of relaxation times analysis of high-temperature PEM fuel cell impedance spectra, Electrochim. Acta 230 (2017) 391–398.
[38] J. Lobato, P. Cañizares, M.A. Rodrigo, F.J. Pinar, E. Mena, D. Úbeda, Three-dimensional model of a 50 cm^2 high temperature PEM fuel cell. Study of the flow channel geometry influence, Int. J. Hydrogen Energy 35 (2010) 5510–5520.
[39] F. Seland, T. Berning, B. Børresen, R. Tunold, Improving the performance of high-temperature PEM fuel cells based on PBI electrolyte, J. Power Sources 160 (2006) 27–36.
[40] H. Sun, H. Chen, Y. Wan, Mass transfer in the HT-PEM fuel cell electrode, Energy Procedia 61 (2014) 1524–1527.
[41] H. Schichlein, A.C. Müller, M. Voigts, A. Krügel, E. Ivers-Tiffée, Deconvolution of electrochemical impedance spectra for the identification of electrode reaction mechanisms in solid oxide fuel cells, J. Appl. Electrochem. 32 (2002) 875–882.
[42] J. Illig, J.P. Schmidt, M. Weiss, A. Weber, E. Ivers-Tiffée, Understanding the impedance spectrum of 18650 LiFePO4-cells, J. Power Sources 239 (2013) 670–679.
[43] F. Ciucci, C. Chen, Analysis of electrochemical impedance spectroscopy data using the distribution of relaxation times: a bayesian and hierarchical bayesian approach, Electrochim. Acta 167 (2015) 439–454.
[44] M. Heinzmann, A. Weber, E. Ivers-Tiffée, Impedance modelling of porous electrode structures in polymer electrolyte membrane fuel cells, J. Power Sources 444 (2019) 227279.
[45] S. Dierickx, A. Weber, E. Ivers-Tiffée, How the distribution of relaxation times enhances complex equivalent circuit models for fuel cells, Electrochim. Acta 355 (2020) 136764.
[46] N. Bevilacqua, R. Gokhale, A. Serov, R. Banerjee, M.A. Schmid, P. Atanassov, et al., Comparing novel PGM-free, platinum, and alloyed platinum catalysts for HT-PEMFCs, ECS Transactions 86 (13) (2018) 221.
[47] K. Yezerska, F. Liu, A. Dushina, O. Sergeev, P. Wagner, A. Dyck, et al., Analysis of the regeneration behavior of high temperature polymer electrolyte membrane fuel cells after hydrogen starvation, J. Power Sources 449 (2020) 227562.
[48] H. Liang, H. Su, B.G. Pollet, V. Linkov, S. Pasupathi, Membrane electrode assembly with enhanced platinum utilization for high temperature proton exchange membrane fuel cell prepared by catalyst coating membrane method, J. Power Sources 266 (2014) 107–113.

[49] H. Su, T.C. Jao, O. Barron, B.G. Pollet, S. Pasupathi, Low platinum loading for high temperature proton exchange membrane fuel cell developed by ultrasonic spray coating technique, J. Power Sources 267 (2014) 155–159.
[50] F. Mack, M. Klages, J. Scholta, L. Jörissen, T. Morawietz, R. Hiesgen, et al., Morphology studies on high-temperature polymer electrolyte membrane fuel cell electrodes, J. Power Sources 255 (2014) 431–438.
[51] F. Mack, T. Morawietz, R. Hiesgen, D. Kramer, V. Gogel, R. Zeis, Influence of the polytetrafluoroethylene content on the performance of high-temperature polymer electrolyte membrane fuel cell electrodes, Int. J. Hydrogen Energy 41 (2016) 7475–7483.
[52] T.H. Wan, M. Saccoccio, C. Chen, F. Ciucci, Influence of the discretization methods on the distribution of relaxation times deconvolution: implementing radial basis functions with DRTtools, Electrochim. Acta 184 (2015) 483–499.
[53] S. Zils, M. Timpel, T. Arlt, A. Wolz, I. Manke, C. Roth, 3D visualisation of PEMFC electrode structures using FIB nanotomography, Fuel Cell. 10 (6) (2010) 966–972.
[54] Quantachrome Instruments: Characterizing Porous Materials and Powders: Gas Sorption System Operating Manual, 2015.
[55] R. Evans, U. Marini Bettolo Marconi, Capillary condensation and adsorption in cylindrical and slit-like pores, J. Chem. Soc., Faraday Trans. 2 82 (1986) 1763–1787.
[56] P.I. Ravikovitch, G.I. Haller, A.V. Neimark, Density functional theory model for calculating pore size distributions: pore structure of nanoporous catalysts, Adv. Colloid Interface Sci. 76–77 (1998) 203–226.
[57] J. Gostick, Versatile and efficient pore network extraction method using marker-based watershed algorithm, Phys. Rev. 96 (2017) 1–15, 023307.
[58] J. Gostick, M. Aghighi, J. Hinebaugh, T. Tranter, M.A. Hoeh, H. Day, et al., OpenPNM: a pore network modeling package, Comput. Sci. Eng. 18 (4) (2016) 60–74.
[59] S. Galbiati, A. Baricci, A. Casalegno, G. Carcassola, R. Marchesi, On the activation of polybenzimidazole-based membrane electrode assemblies doped with phosphoric acid, Int. J. Hydrogen Energy 37 (2012) 14475–14481.
[60] L. Dubau, M. Lopez-Haro, L. Castanheira, J. Durst, M. Chatenet, P. Bayle-Guillemaud, et al., Probing the structure, the composition and the ORR activity of Pt3Co/C nanocrystallites during a 3422 h PEMFC ageing test, Appl. Catal. B Environ. 142–143 (2013) 801–808.
[61] V.R. Stamenkovic, B.S. Mun, K.J.J. Mayrhofer, P.N. Ross, N.M. Markovic, Effect of surface composition on electronic structure, stability, and electrocatalytic properties of Pt-transition metal alloys: Pt-skin versus Pt-skeleton surfaces, J. Am. Chem. Soc. 128 (27) (2006) 8813–8819.
[62] S. Koh, J. Leisch, M.F. Toney, P. Strasser, Structure-activity-Stability relationships of Pt-Co electrocatalysts in gas-diffusion electrode layers, J. Phys. Chem. C 111 (2007) 3744–3752.
[63] S. Ohyagi, T. Sasaki, Durability of a PEMFC Pt-Co cathode catalysts layer during voltage cycling tests under supersaturated humidity conditions, Electrochim. Acta 102 (2013) 336–341.
[64] U.A. Paulus, A. Wokaun, G.G. Scherer, Oxygen reduction on carbon-supported Pt-Ni and Pt-Co alloy catalysts, J. Phys. Chem. B 106 (2002) 4181–4191.
[65] V. Stamenković, T.J. Schmidt, P.N. Ross, N.M. Marković, Surface composition effects in electrocatalysis: kinetics of oxygen reduction on well-defined Pt3Ni and Pt3Co alloy surfaces, J. Phys. Chem. B 106 (2002) 11970–11979.